The domain of unknown function 4005 (DUF4005) in an *Arabidopsis* IQD protein functions in microtubule binding

Yan Li[1], Yujia Huang[1], Yunze Wen[1], Dan Wang[1], Haofeng Liu[1], Yuanfeng Li[1], Jun Zhao[1], Lijun An[1], Fei Yu[1,2], and Xiayan Liu[1,*]

From the [1]State Key Laboratory of Crop Stress Biology for Arid Areas and College of Life Sciences, [2]Institute of Future Agriculture, Northwest A&F University, Yangling, Shaanxi, People's Republic of China

Edited by Joseph Jez

The dynamic responses of microtubules (MTs) to internal and external signals are modulated by a plethora of microtubule-associated proteins (MAPs). In higher plants, many plant-specific MAPs have emerged during evolution as advantageous to their sessile lifestyle. Some members of the IQ67 domain (IQD) protein family have been shown to be plant-specific MAPs. However, the mechanisms of interaction between IQD proteins and MTs remain elusive. Here we demonstrate that the domain of unknown function 4005 (DUF4005) of the *Arabidopsis* IQD family protein ABS6/AtIQD16 is a novel MT-binding domain. Cosedimentation assays showed that the DUF4005 domain binds directly to MTs *in vitro*. GFP-labeled DUF4005 also decorates all types of MT arrays tested *in vivo*. Furthermore, we showed that a conserved stretch of 15 amino acid residues within the DUF4005 domain, which shares sequence similarity with the C-terminal MT-binding domain of human MAP Kif18A, is required for the binding to MTs. Transgenic lines overexpressing the DUF4005 domain displayed a spectrum of developmental defects, including spiral growth and stunted growth at the organismal level. At the cellular level, DUF4005 overexpression caused defects in epidermal pavement cell and trichome morphogenesis, as well as abnormal anisotropic cell elongation in the hypocotyls of dark-grown seedlings. These data establish that the DUF4005 domain of ABS6/AtIQD16 is a new MT-binding domain, overexpression of which perturbs MT homeostasis in plants. Our findings provide new insights into the MT-binding mechanisms of plant IQD proteins.

Microtubules (MTs) are polymers assembled by α- and β-tubulin dimers and play critical roles in determining cell shape, cell polarity, intracellular transport, and cell division in eukaryotic cells. Given the sessile nature of terrestrial plants and the restriction of cell movement by the cell wall, dynamic responses of MTs are essential for higher plants to respond to the developmental and environmental cues (1–4).

During plant cell cycles, MTs adopt several different types of arrays. In interphase cells, distinct cortical MT (cMT) organizations are formed depending on the specific developmental stage and physiological state of the plant cell (1). cMTs are closely associated with the cell membrane, where they serve as tracks for cellulose synthases (CESAs) (5–7). Plant cells undergoing rapid anisotropic growth typically display transverse cMT arrays that are perpendicular to the direction of elongation (8). Specialized cells such as trichomes, guard cells, and pavement cells all have their signature patterns of MT organizations (1). In dividing cells, before entering mitosis, MTs are part of a ring-like structure called preprophase band (PPB) at the cell cortex, which forecasts the position of the future cell division plane (9). In mitosis, like in other eukaryotic cells, MTs form the conserved spindle structure, ensuring the faithful separation of chromosomes (10). During cytokinesis, MTs are the major component of the phragmoplast, a plant-specific structure that directs the assembly of the cell plate and the new cell wall between daughter cells (11).

To date, a broad spectrum of microtubule-associated proteins (MAPs) have been identified in animal and plant cells (12). MAPs modulate many aspects of MT dynamics, such as nucleation, severing, polymerizing, and bundling, underpinning the robust response of MTs to external and internal cues (12, 13). Many MAP families were conserved across kingdoms of life, such as the MT severing enzyme katanin, the MT polymerase MAP215, the kinesin motors, the augmin complex, and the MT plus-end tracking protein EB1 (13). In addition, an increasing number of plant-specific MAPs have been identified, highlighting a complex complement of MAPs in plants (1, 13). For example, CELLULOSE SYNTHASE INTERACTING1/POM-POM2 (CSI1/POM2), a novel plant MAP, was identified in a yeast two-hybrid screen for interacting partners of CESA, and CSI1 functions as bridges between the CESA complexes and cMTs during cellulose biosynthesis (6, 14). Genetic lesions in plant MAP coding genes often perturb MT dynamics and organization, cause defects in anisotropic cell expansion, and eventually lead to abnormal cell and organ morphogenesis, such as impaired hypocotyl elongation and altered morphogenesis of leaf epidermal pavement cells and trichomes (13). In loss-of-function mutants of the *Arabidopsis KATANIN1* (*KTN1*) gene, encoding the p60 catalytic subunit of the MT severing enzyme katanin, MTs are highly disorganized and unable to form ordered parallel arrays in elongating hypocotyl cells (15, 16). Consequently, *ktn1*

mutants have shortened hypocotyls, reduced trichome branching number, and smaller pavement cells with less prominent indentations (15–17). Many plant MAPs are members of protein families, which suggests that conserved family members may share redundant functions. For example, *Arabidopsis* TON1 recruiting motif (TRM) family members TRM6, 7, and 8 collectively control the formation of PPB and the precision of cell division orientation (9).

The plant-specific IQ67 domain (IQD) family proteins were defined by the presence of a conserved IQ67 domain of 67 amino acid residues (18). The IQ67 domain harbors 1 to 3 tandem repeats of calmodulin-binding IQ motifs, each containing two conserved isoleucine (I) and glutamine (Q) amino acid residues (18). Among the 33 known IQD family members in *Arabidopsis thaliana*, only a few have been functionally characterized. Among them, AtIQD1 has been shown to localize to both the nucleus and cMTs and interacts with kinesin light chain-related protein-1 (KLCR1) (19). AtIQD13 associates with both the plasma membrane and MTs to regulate the formation of secondary cell wall pits in xylem cells (20). Mutations in *AtIQD5* lead to altered pavement cell morphology and render plants hypersensitive to an MT-destabilizing drug oryzalin (21, 22). Our previous study found that ABNORMAL SHOOT 6 (ABS6)/AtIQD16 promotes cMT severing and ordering through a direct interaction with KTN1 (23). Despite an increasing body of evidence suggesting that at least a subset of IQD proteins function as MAPs in plants, the interacting mechanisms between IQD proteins and MTs remain unclear.

In this study, we determined that the DUF4005 domain of ABS6/AtIQD16 is a novel MT-binding domain in plants. We showed that the DUF4005 domain, a peptide of 59 amino acids, binds directly to MTs *in vitro*. Fluorescent protein-labeled DUF4005 domain decorates all types of MT arrays *in planta*. We further demonstrated that a conserved region of 15 amino acid residues in DUF4005 is indispensable for MT binding. Moreover, the overexpression of the DUF4005 domain leads to a spectrum of developmental defects associated with the perturbation of MT homeostasis and abnormal cell morphogenesis. These findings provide new insight into our understanding of the molecular basis of MT binding in *Arabidopsis* IQD proteins.

Results

Domain of unknown function 4005 (DUF4005) is an MT-binding domain in ABS6

ABS6 is an *Arabidopsis* IQD family protein, which is also designated AtIQD16 (18). In the full-length ABS6 amino acid sequences, conserved domain search identified two IQ motifs (amino acid residues 100–120 and 123–141, respectively), a coiled coil motif (residues 231–251), and a Domain of Unknown Function 4005 (DUF4005) (residues 329–387) (Fig. 1A). Previously, we have shown that a GFP fusion of the N-terminal region (amino acid residues 1–200) of ABS6 does not associate with MTs in *Arabidopsis* protoplasts (23). We have also demonstrated a direct MT-binding capability for the

C-terminal region (residues 201–423) of ABS6, establishing ABS6/AtIQD16 as a *bona fide* MAP (23). To identify the potential MT-binding domain in ABS6, we generated a series of truncated forms of the C-terminal region of ABS6 fused at their C-termini with GFP (Fig. 1A). Among them, ABS6$^{329-387}$ corresponds to the DUF4005 domain (Fig. 1A). Next we determined their cellular localizations by transiently expressing these GFP fusions in mesophyll protoplasts from an *Arabidopsis* MT marker line, *mRFP-TUB6* (Fig. 1B) (24). Among the different forms of ABS6, ABS6$^{329-387}$-GFP, as well as the longer versions ABS6$^{201-423}$-GFP and ABS6$^{301-423}$-GFP showed GFP fluorescent signals that overlapped with RFP signals from mRFP-TUB6, whereas ABS6$^{387-423}$-GFP showed diffused GFP signals in the cytosol (Fig. 1B). These data suggest that the DUF4005 domain colocalizes with cMTs and may mediate the association between ABS6 and cMTs.

To test whether the DUF4005 domain could bind directly to MTs, we performed the *in vitro* MT cosedimentation assay. N-terminal glutathione S-transferase (GST)-tagged recombinant ABS6$^{329-387}$(GST-ABS6$^{329-387}$) or GST was incubated with taxol-stabilized MTs. When incubated with MTs, GST was mostly found in the supernatant after ultracentrifugation, while MTs were sedimented in the pellet fraction, indicating that GST is not associated with MTs (Fig. 2A). In contrast, GST-ABS6$^{329-387}$ was present in the pellet after incubation and centrifugation, together with MTs (Fig. 2A). Moreover, the amount of GST-ABS6$^{329-387}$ in the pellet increased as the input of GST-ABS6$^{329-387}$ increased in the incubation (Fig. 2A).

To determine the binding affinity of GST-ABS6$^{329-387}$ for taxol-stabilized MTs, We performed additional MT cosedimentation assays with a fixed concentration of MTs and increasing concentrations of GST-ABS6$^{329-387}$. The binding affinity of GST-ABS6$^{329-387}$ for taxol-stabilized MTs was estimated based on the quantification of MT-bound GST-ABS6$^{329-387}$ and free GST-ABS6$^{329-387}$ in each cosedimentation assay. Data were fit to the bimolecular binding curve (Fig. 2B). A K_d of 0.996 ± 0.147 μM was estimated for the binding of GST-ABS6$^{329-387}$ to MTs (Fig. 2B). These data confirmed that ABS6$^{329-387}$ binds to MTs. Finally, we asked whether ABS6$^{329-387}$ could interact with free tubulins. In pull-down assays, tubulin was incubated with GST- or GST-ABS6$^{329-387}$-bound glutathione beads. After elution, both tubulin and GST-ABS6$^{329-387}$ were detected in the pull-down fraction, whereas the interaction between tubulin and GST alone was not detected, indicating that ABS6$^{329-387}$ is able to bind tubulin (Fig. 2C). Taken together, we establish the DUF4005 domain of ABS6/IQD16 as an MT-binding domain.

A conserved motif in DUF4005 is necessary for MT binding

We identified 21 proteins in *Arabidopsis* containing the DUF4005 domain in the Pfam database, all of which belong to the IQD family (Fig. 3A). These DUF4005-containing IQD proteins shared conserved domain arrangements, including one or two IQ motifs in the N-terminal region and one DUF4005 domain in the C-terminal region (Fig. 3A). Next, we
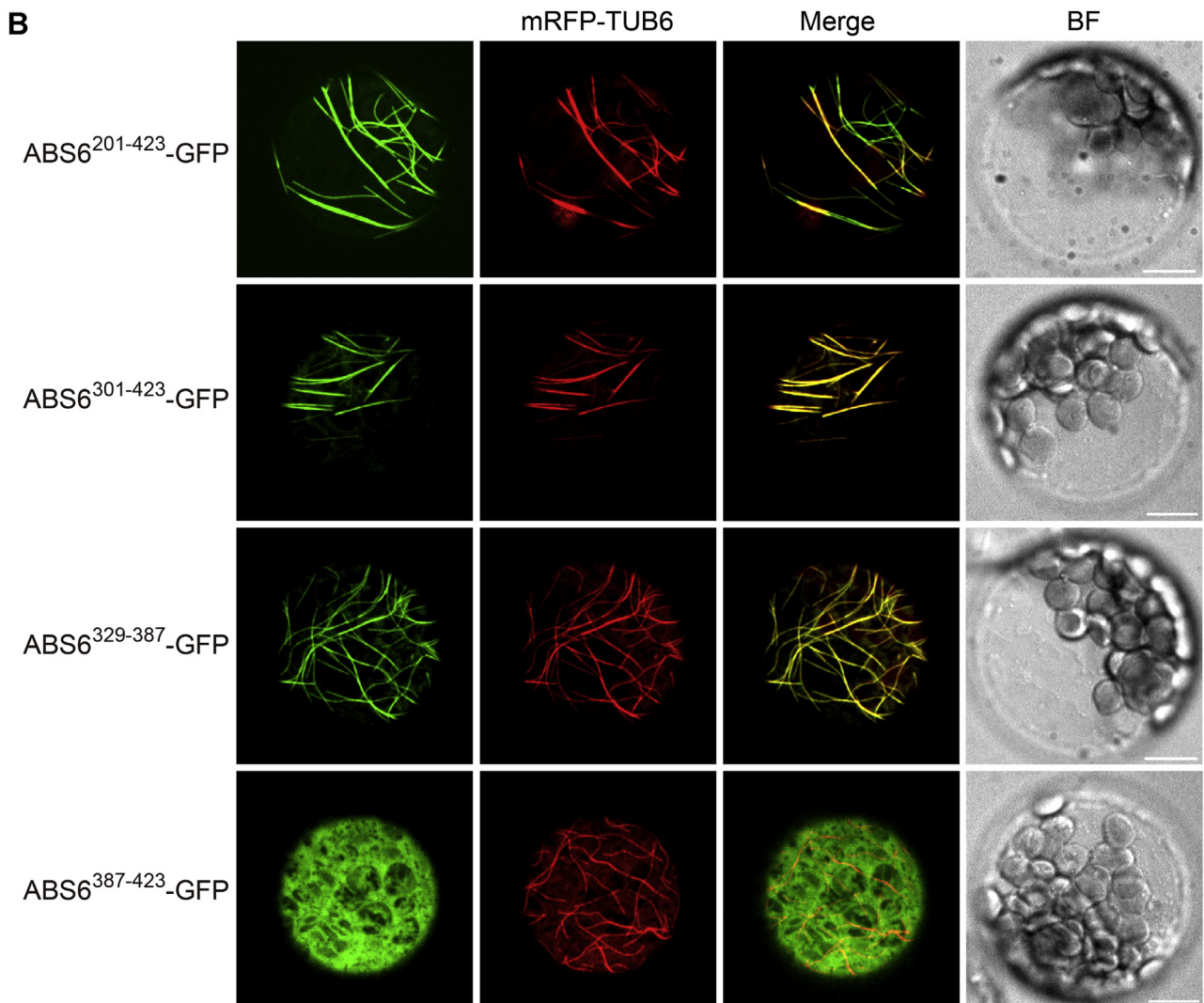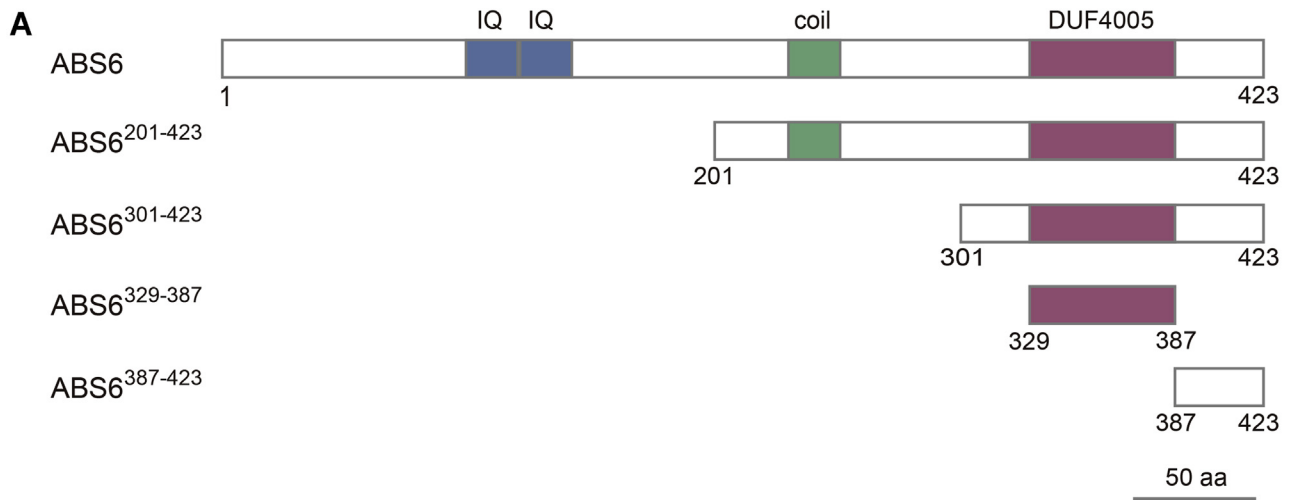
Figure 1. Identification of the MT-binding domain in ABS6. *A*, schematic representations of truncated forms of ABS6 used in this study. *B*, imaging of GFP fusions of truncated ABS6 and mRFP-TUB6 in living protoplasts. GFP fusions of truncated ABS6 were transiently expressed in protoplasts from the *mRFP-TUB6* line. Bars: 10 μm. coil, coiled coil motif; DUF4005, domain of unknown function 4005; IQ, calmodulin-binding IQ motif.

A

B

$K_d = 0.996 \pm 0.147$ µM

C
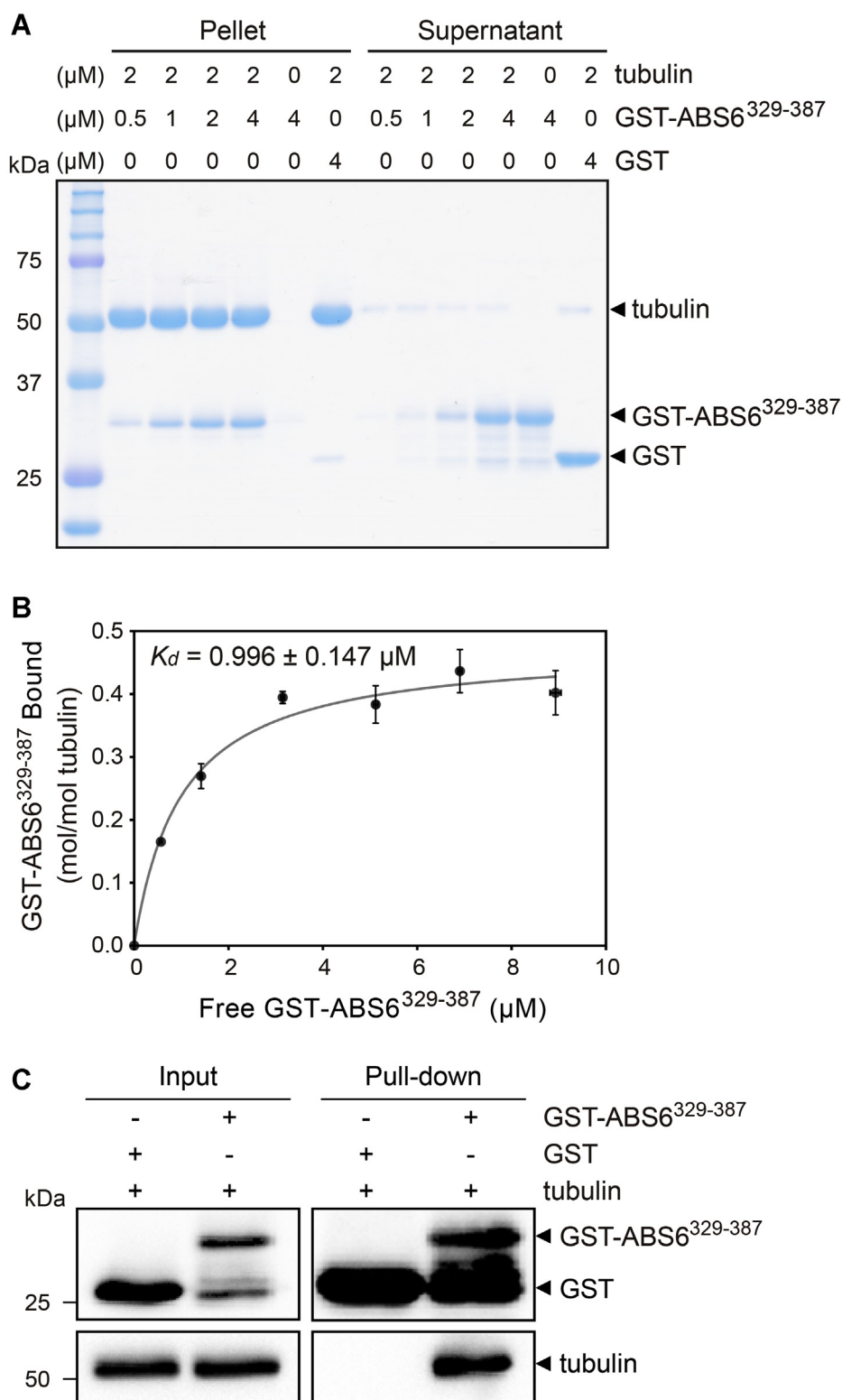
Figure 2. ABS6[329–387] directly binds to MTs and tubulin dimers. *A*, cosedimentation of GST-ABS6[329–387] with taxol-stabilized MTs *in vitro*. Different concentrations (0, 0.5, 1, 2, and 4 µM) of GST-ABS6[329–387] were incubated with taxol-stabilized MTs equivalent to 2 µM tubulin and sedimented with ultracentrifugation. Pellets (P) and supernatants (S) were analyzed by SDS-PAGE followed by Coomassie Blue staining. GST served as a negative control. *B*, estimation of the binding affinity of GST-ABS6[329–387] for taxol-stabilized MTs. Various concentrations (0, 1, 2, 4, 6, 8, and 10 µM) of GST-ABS6[329–387] were cosedimented with taxol-stabilized MTs equivalent to 2 µM tubulin. The amounts of MT-bound GST-ABS6[329–387] and free GST-ABS6[329–387] were calculated based on band intensities on SDS-PAGE gels and used to estimate K_d value. See Experimental procedures for details. Data points are means ± standard deviation (s.d.) of three biological replicates. *C*, direct interaction of GST-ABS6[329–387] and tubulin in pull-down assays. GST-ABS6[329–387]- or GST-bound glutathione beads were incubated with tubulin, washed, and eluted. Inputs and elutes were analyzed by immunoblotting with anti-GST and anti-tubulin antibodies.
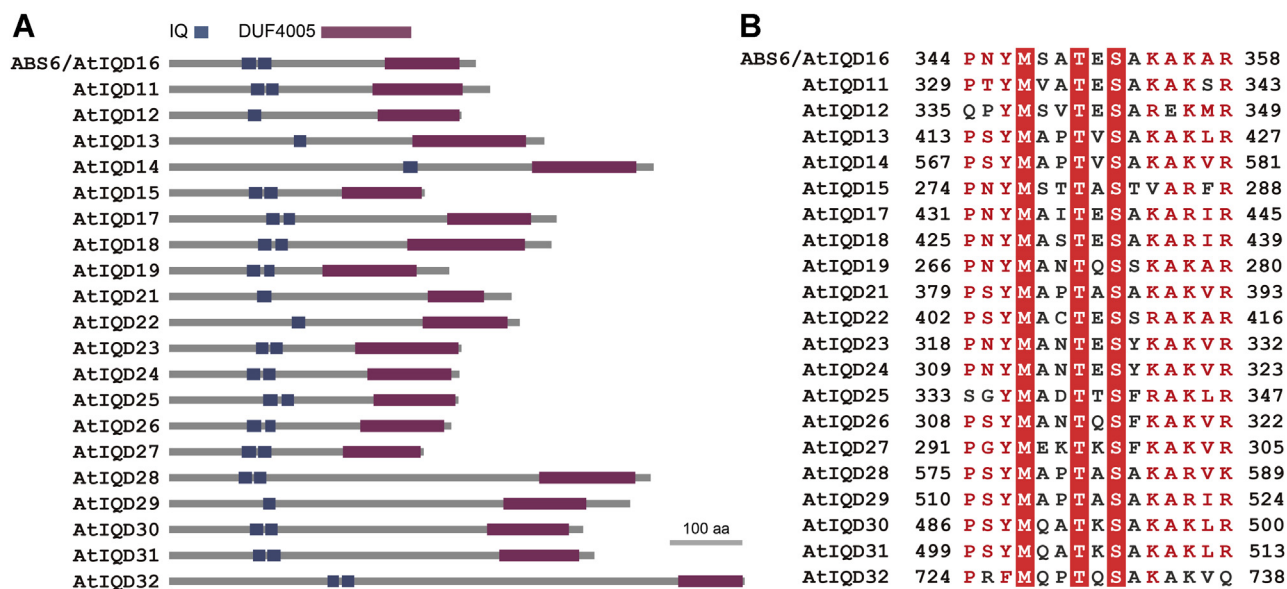
Figure 3. DUF4005 is present in a subset of IQD proteins in *Arabidopsis*. *A*, domain architecture of AtIQDs containing the DUF4005 domain. *B*, sequence alignment of the most conserved region in DUF4005 of AtIQDs. Sequences of the DUF4005 domain in *Arabidopsis* IQD proteins were aligned with the Clustal Omega tool (https://www.ebi.ac.uk/Tools/msa/clustalo/). Color-coded figure of protein sequence alignment was generated with ESPript 3.0 (https://espript.ibcp.fr/ESPript/cgi-bin/ESPript.cgi).

sought to identify key amino acids that are essential for MT binding in DUF4005. Multiple alignments of DUF4005 sequences of *Arabidopsis* IQD proteins revealed that a region encompassing proline 344 to arginine 358 in ABS6 is highly conserved (Fig. 3B). To test whether this conserved motif is required for MT binding, we generated three mutated versions of ABS6$^{329-387}$, designated Δ(P-R), Δ(P-S), and Δ(K-R). In Δ(P-R), the entire conserved region from P344 to R358 was deleted (Fig. 4A). Shorter deletions, from P344 to S352 and from K354 to R358 were generated as Δ(P-S) and Δ(K-R), respectively (Fig. 4A). In cosedimentation assays, GST-Δ(P-S) could still bind to MTs, whereas binding of GST-Δ(P-S) and GST-Δ(K-R) to MTs was hardly detectable (Fig. 4B). These findings suggest that the residues from K354 to R358 were indispensable for MT binding *in vitro*. Next, we investigated whether the mutated versions of DUF4005 could associate with MTs in plant cells by expressing Δ(P-R)-GFP, Δ(P-S)-GFP, and Δ(K-R)-GFP fusion proteins in *mRFP-TUB6* protoplasts, respectively. Consistent with their inability to bind MTs *in vitro*, Δ(P-R)-GFP and Δ(K-R)-GFP yielded diffused GFP signals in cytosol that were not associated with mRFP-labeled MTs (Fig. 4C). However, despite the apparent MT binding of Δ(P-S) in cosedimentation assays, overall the MT signals for Δ(P-S)-GFP were weak and the majority of Δ(P-S)-GFP signals were diffused in the cytosol, suggesting that residues from P344 to S352 are required for efficient MT binding *in vivo* (Fig. 4C). Together, these results suggest that a conserved motif from P344 to R358 in the DUF4006 domain of ABS6 is necessary for MT binding.

The role of the DUF4005 domain in MT binding prompted us to search for similar motifs among other MAPs. Surprisingly, we identified similar sequences between the conserved region in DUF4005 and the MT-binding domain in the

C-terminal tail of human Kif18A. Residing within the last 100 amino acid residues of Kif18A, the C-terminal MT-binding domain of Kif18A has a high affinity for MTs and binds to MTs in an ATP-independent manner (25, 26). We retrieved additional sequences of Kif18A homologs from various animal species, and the C-terminal tails are highly conserved among Kif18A homologs in vertebrates (Fig. 4D). Partial alignments between sequences of C-terminal tails of Kif18A homologs and the DUF4005 domain of ABS6 revealed that residues between P344 and R358 in ABS6 are highly similar in Kif18A homologs in vertebrates, including zebrafish (*Danio rerio*), African Clawed Frog (*Xenopus laevis*), chicken (*Gallus gallus*), and several mammals (Fig. 4D), suggesting it may represent a common MT-binding motif shared by different types of MAPs.

The DUF4005 domain binds to MTs through electrostatic interactions

One common mechanism of MAP-MT interaction is through the electrostatic interaction between the basic domain of MAPs and the acidic C-terminal tail (E-hook) of tubulin (27). The conserved region essential for MT-binding in ABS6$^{329-387}$ is highly basic (Figs. 3 and 4). If the binding of ABS6$^{329-387}$ to MTs is dependent on electrostatic interactions, we should be able to observe dissociation of ABS6$^{329-387}$ from MTs at high salt concentrations. Indeed, in cosedimentation assays carried out at different NaCl concentrations, the MT-binding ability of GST-ABS6$^{329-387}$ decreased as the concentration of NaCl increased (Fig. 5, A and B). At 100 mM NaCl, the level of MT-bound GST-ABS6$^{329-387}$ was reduced to ~45% of that at 0 mM NaCl while 250 mM or 500 mM NaCl almost completely prevented the binding of ABS6$^{329-387}$ to MTs (Fig. 5, A and B). In addition, we subjected MTs to limited proteolysis with subtilisin to remove the tubulin
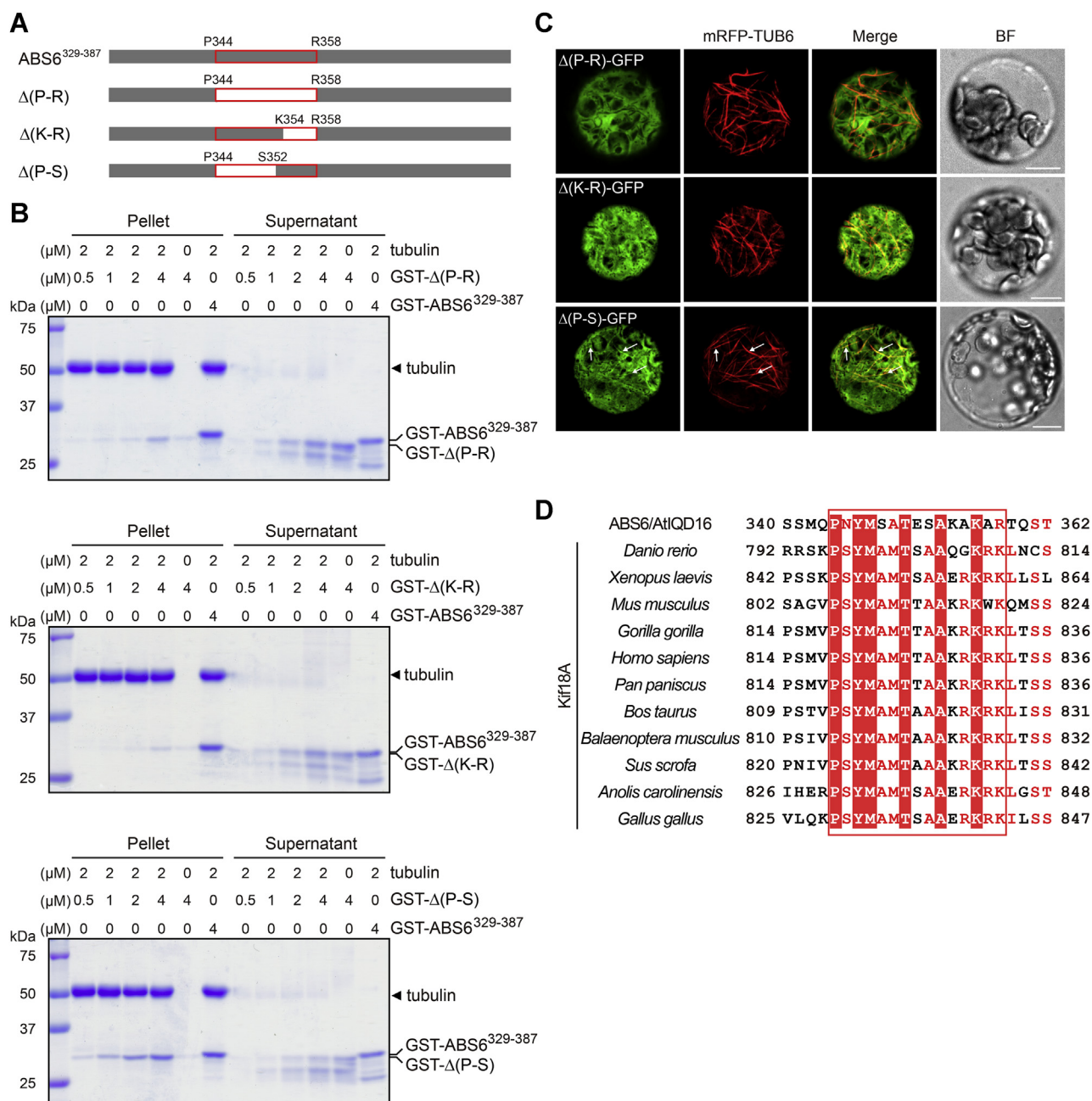
Figure 4. A conserved region in DUF4005 is necessary for MT binding. *A*, schematic representations of the mutated versions of ABS6$^{329-387}$ used in MT-binding analyses. *Red framed boxes* indicated the conserved region from P344 to R358. *White boxes* indicated deleted regions. Δ(P-R), P344–R358, was deleted; Δ(K-R), K354–R358, was deleted; Δ(P-S), P344–S352, was deleted. *B*, cosedimentation of GST-Δ(P-R), GST-Δ(K-R), and GST-Δ(P-S) with taxol-stabilized MTs *in vitro*. Cosedimentation assays were performed as in Figure 2A. GST served as a negative control. *C*, imaging of GFP fusions of mutated versions of ABS6$^{329-387}$ and mRFP-TUB6 in living protoplasts. Δ(P-R)-GFP, Δ(K-R)-GFP, and Δ(P-S)-GFP were transiently expressed in protoplasts from the *mRFP-TUB6* line. *White arrows* pointed to the overlapped signals of Δ(P-S)-GFP and mRFP-TUB6. Bar:10 μm. *D*, partial sequence alignment of ABS6 DUF4005 and the C-terminal MT-binding region of Kif18A from various species. Sequences were aligned as in Figure 3B. Kif18A homologs used in the alignment are *Danio rerio*, NP_956533; *Xenopus laevis*, XP_018112945; *Mus musculus*, NP_647464; *Gorilla gorilla*, XP_004050908; *Homo sapiens*, NP_112494; *Pan paniscus*, XP_003830477; *Bos taurus*, NP_001179838; *Balaenoptera musculus*, XP_036717440; *Sus scrofa*, XP_003122951; *Anolis carolinensis*, XP_003225678; *Gallus gallus*, NP_001186355.

C-terminal tails (28). SDS-PAGE analysis showed that subtilisin-treated MTs migrated as two bands, verifying the partial removal of the tubulin C-terminal tail (Fig. 5C). The amount of GST-ABS6$^{329-387}$ cosedimented with subtilisin-treated MTs was markedly reduced compared with that cosedimented with mock-treated MTs (Fig. 5, *C* and *D*). Together, these data suggest that ABS6$^{329-387}$ likely binds MTs

through electrostatic interactions with the C-terminal tail of tubulin.

Overexpression of the DUF4005 domain of ABS6 alters cell morphogenesis in Arabidopsis

Since the DUF4005 domain of ABS6 is capable of direct MT binding, it is possible that ectopic expression of this domain
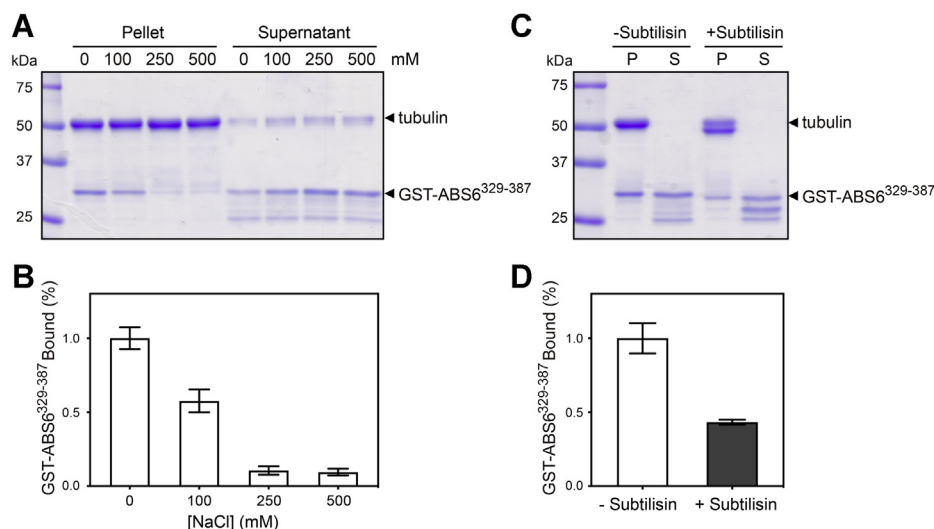
Figure 5. ABS6$^{329-387}$ binds to MTs through electrostatic interactions with the C-terminal tail of tubulin. *A*, cosedimentation of GST-ABS6$^{329-387}$ with taxol-stabilized MTs at different NaCl concentrations. Cosedimentation assays were carried out as in Figure 2*A*. *B*, quantifications of the effect of NaCl on the binding of GST-ABS6$^{329-387}$ to MTs. Intensities of GST-ABS6$^{329-387}$ bands in pellets were normalized to intensities of tubulin bands in pellets. The relative level of GST-ABS6$^{329-387}$ in pellets at 0 mM NaCl was defined as 100%. *C*, cosedimentation of GST-ABS6$^{329-387}$ with mock-treated MTs or subtilisin-treated MTs. Taxol-stabilized MTs were incubated with subtilisin or equal amount of buffer for 90 min prior to cosedimentation assays. *D*, quantification of the effect of subtilisin treatment on the binding of GST-ABS6$^{329-387}$ to MTs. The relative level of GST-ABS6$^{329-387}$ cosedimented with mock-treated MTs was defined as 100%. In *B* and *D*, data are means ± s.d. of three biological replicates.

may affect MT homeostasis and plant development. To this end, we transformed constitutive 35S promoter-driven *ABS6$^{329-387}$-GFP* fusion gene into the WT background and generated stable transgenic lines (Fig. 6*A*). A range of developmental defects were observed in *ABS6$^{329-387}$-GFP* overexpression (OE) lines, and these lines were placed into weak, moderate, and strong categories based on the severity of growth abnormalities (Fig. 6*A*). Weak *ABS6$^{329-387}$-GFP* OE lines were mostly indistinguishable from WT when grown in soil (Fig. 6*A*). Interestingly, moderate *ABS6$^{329-387}$-GFP* OE lines displayed pronounced left-handed helical growth, whereas strong *ABS6$^{329-387}$-GFP* OE lines led to severely stunted growth (Fig. 6*A*). The severity of developmental defects in *ABS6$^{329-387}$-GFP* OE lines correlated with the levels of *ABS6$^{329-387}$* transcripts, with higher *ABS6$^{329-387}$* expressions associated with stronger growth defects (Fig. 6, *A* and *B*).

Next, we examined the impact of ectopic expression of *ABS6$^{329-387}$-GFP* on cell morphogenesis and examined leaf epidermal pavement cells and trichomes. WT pavement cells showed the stereotypical "jigsaw" puzzle shape with interlocked lobes and indentations, and WT trichomes typically have three or four straight branches (Fig. 6, *C* and *D*). In agreement with the overall weak growth phenotype, pavement cells and trichomes in weak *ABS6$^{329-387}$-GFP* OE lines were similar in shapes to those in the WT (Fig. 6, *C* and *D*). In moderate *ABS6$^{329-387}$-GFP* OE lines, pavement cells were smaller and had fewer number of lobes, compared with those in WT (Fig. 6*C*). Trichomes maintained their overall shapes in moderate *ABS6$^{329-387}$-GFP* OE lines, but they appeared curly, in contrast to the straight branches in WT trichomes (Fig. 6*D*). Surprisingly, in strong *ABS6$^{329-387}$-GFP* OE lines, both pavement cells and trichomes were drastically different from those in WT (Fig. 6, *C* and *D*). Pavement cells in strong *ABS6$^{329-387}$-GFP* OE

lines lost the conspicuous lobes and indentations found in WT pavement cells and instead showed much smooth cell outlines with only few shallow outgrowths (Fig. 6*C*). Trichome branch numbers were clearly increased, and trichomes with five or more branches were commonly observed in strong *ABS6$^{329-387}$-GFP* OE lines (Fig. 6*D*). In addition to increased branch numbers, trichome branches often showed small bulges or outgrowths in strong *ABS6$^{329-387}$-GFP* OE lines (Fig. 6*D*). These findings suggest that the overexpression of the MT-binding DUF4005 domain of ABS6 is capable of modulating cell morphogenesis in Arabidopsis.

Overexpression of ABS6$^{329-387}$-GFP *alters anisotropic cell expansion in hypocotyls of dark-grown seedlings*

Interphase cMT arrays are intimately linked to anisotropic cell expansion (1, 13). To determine the impact of the overexpression of the DUF4005 domain on anisotropic cell expansion and cMT organization, we crossed *ABS6$^{329-387}$-GFP* into the MT marker line *mRFP-TUB6*. We focused on the hypocotyl of dark-grown seedlings, a canonical model for anisotropic cell elongation, for our analysis. Consistent with overall growth defects, weak, moderate, and strong *ABS6$^{329-387}$-GFP* OE lines with increasingly more severe hypocotyl elongation defects in the *mRFP-TUB6* background were identified (Fig. 7, *A* and *B*). Weak *ABS6$^{329-387}$-GFP* OE lines showed comparable hypocotyl growth and hypocotyl epidermal cell shape as those in the *mRFP-TUB6* line (Fig. 7, *A* and *B*). At the molecular level, cMT patterns in weak OE lines also resembled those of *mRFP-TUB6* (Fig. 7*C*). ABS6$^{329-387}$-GFP signals merged well with mRFP-TUB6 signals, indicating an association of DUF4005 with MTs *in vivo* (Fig. 7*C*). Hypocotyls of moderate *ABS6$^{329-387}$-GFP* OE lines were modestly shorter than those of the *mRFP-TUB6* lines (Fig. 7*A*).
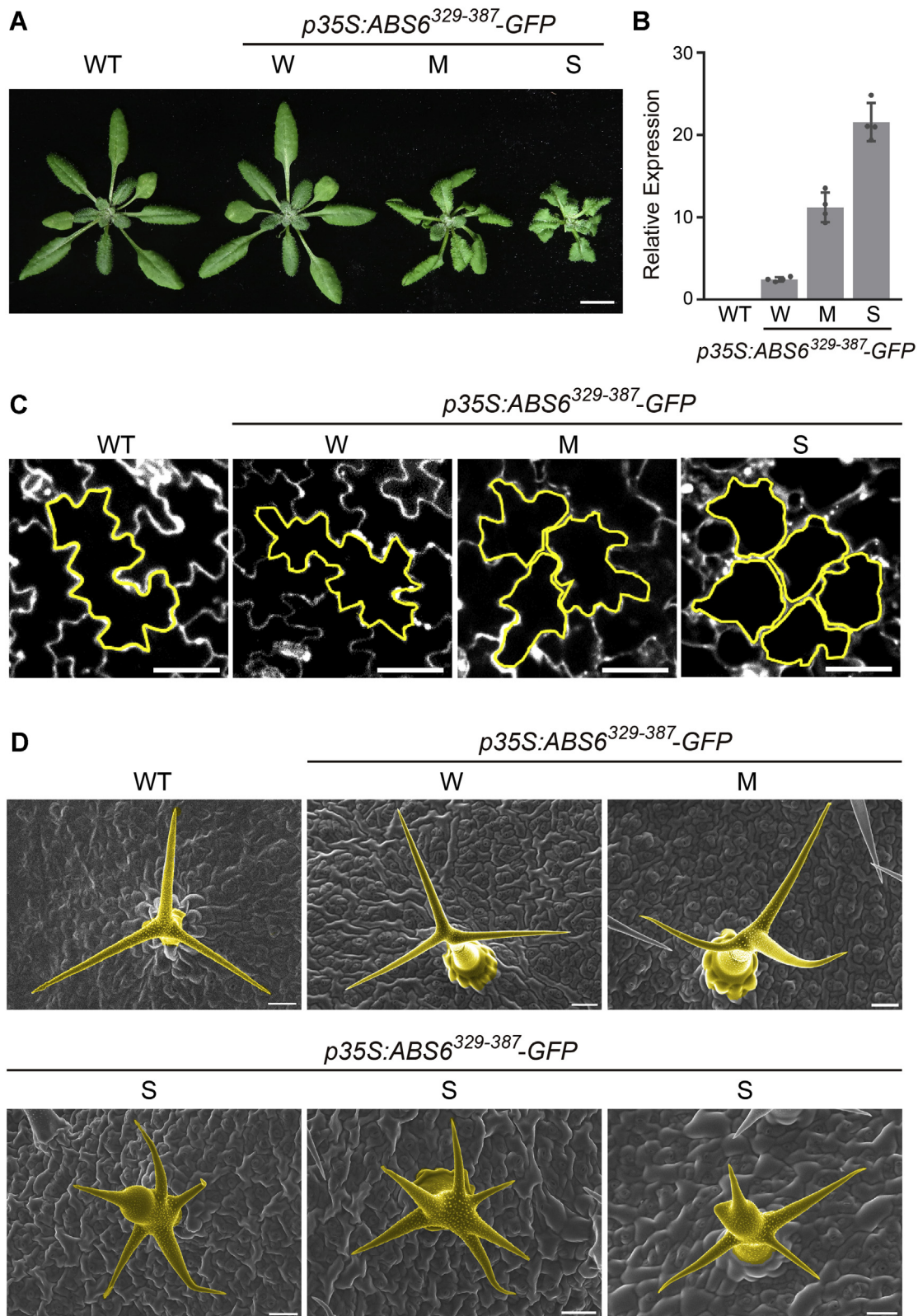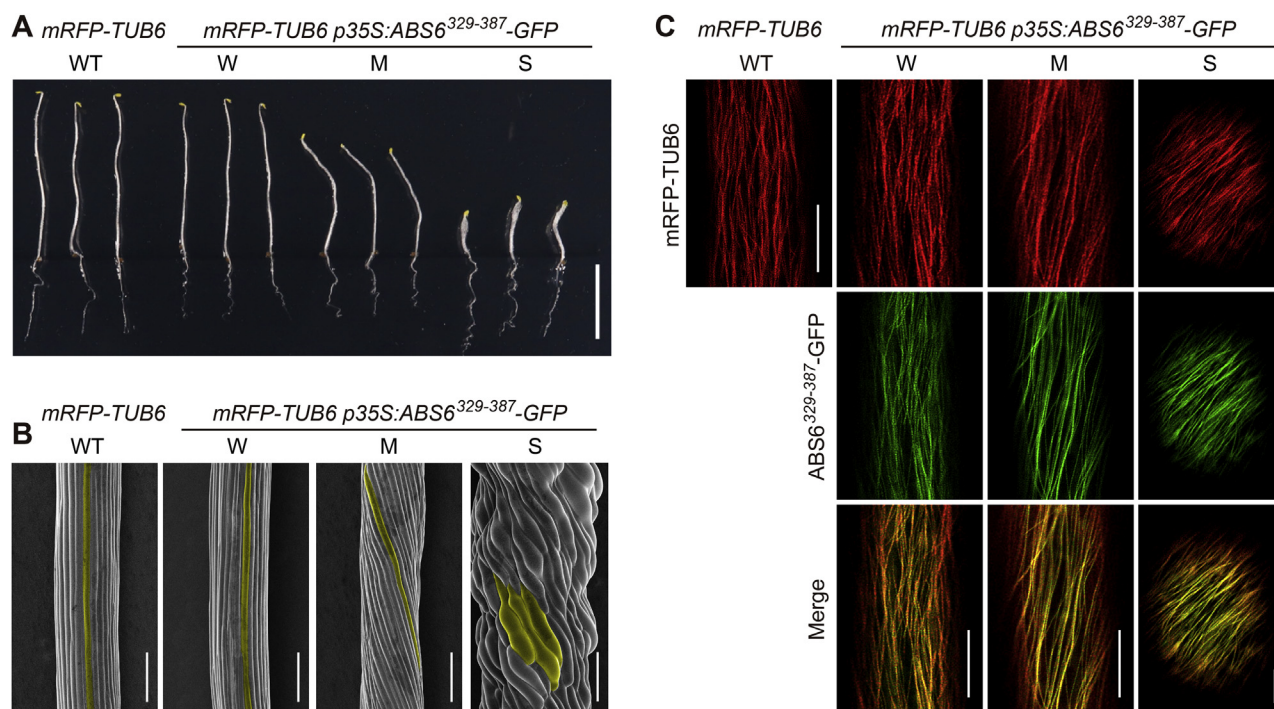
Figure 6. Phenotypic analysis of *ABS6*^{329–387}-GFP OE lines. *A*, rosettes of 3-week-old WT, and representative weak, moderate, and strong *ABS6*$^{329-387}$-*GFP* OE lines. Bars: 1 cm. *B*, RT-qPCR analyses of *ABS6*$^{329-387}$-*GFP* transcript levels in plants shown in *A*. Relative expressions were calculated with respected to the *ACT2* expressions. Data are means ± s.d. of three biological replicates. *C*, pavement cell morphology in WT, and representative weak, moderate, and strong *ABS6*$^{329-387}$-*GFP* OE lines. Imaged were the abaxial side of cotyledons in 1-week-old seedlings. Bars: 50 μm. *D*, scanning electron micrographs of typical trichomes in WT, and representative weak, moderate, and strong *ABS6*$^{329-387}$-*GFP* OE lines. Bars: 50 μm.

Figure 7. Overexpression of *ABS6^329−387^-GFP* affects anisotropic cell expansion in hypocotyls of dark-grown seedlings. *A*, hypocotyl elongation in 6-day-old dark-grown seedlings of WT, and representative weak, moderate, and strong *ABS6^329−387^-GFP* OE lines in the *mRFP-TUB6* background. Bar: 1 cm. *B*, scanning electron micrographs of hypocotyl epidermal cells. Bars: 200 μm. A representative epidermal cell in the hypocotyl was highlighted in yellow in each graph. Note that in WT and weak *ABS6^329−387^-GFP* OE lines, hypocotyl epidermal cells highlighted in the graph were not intact since their lengths were longer than that of the graph. *C*, confocal imaging of cMT arrays in hypocotyl epidermal cells. Bars: 10 μm. Six-day-old dark-grown seedlings of the same genotypes as shown in *A* were used for imaging in *B* and *C*.

Notably, hypocotyls of moderate *ABS6^329−387^-GFP* OE lines were not straight, but inclined toward the left (Fig. 7A). A clear left-handed helical pattern of hypocotyl epidermal cell files was found in moderate *ABS6^329−387^-GFP* OE lines (Fig. 7B). Consistently with the left-handed twisting, cMTs arrays were oblique in hypocotyl epidermal cells of moderate *ABS6^329−387^-GFP* OE lines, in contrast to the longitudinal cMTs arrays in the *mRFP-TUB6* and weak *ABS6^329−387^-GFP* OE lines (Fig. 7C). In strong *ABS6^329−387^-GFP* OE lines, hypocotyls were much thicker than those of the WT or the weak and moderate *ABS6^329−387^-GFP* OE lines (Fig. 7A). In these lines, hypocotyl epidermal cells were short and distorted and also displayed a left-handed helical pattern (Fig. 7B). Consistent with the stronger cellular phenotype, cMT arrays in hypocotyl epidermal cells of strong *ABS6^329−387^-GFP* OE lines tilted to a greater degree than those of the moderate *ABS6^329−387^-GFP* OE lines (Fig. 7, *B* and *C*). In all *ABS6^329−387^-GFP* OE lines, ABS6^329−387^-GFP was found to decorate cMTs, overlapping with MTs indicated by mRFP-TUB6 (Fig. 7C). Together, these data reinforce that *ABS6^329−387^-GFP* could associate with MTs, perturb MT homeostasis, and eventually alter cell morphogenesis.

### ABS6^329−387^-GFP labels the four types of MT arrays in planta

In plants, MTs exist as cMT, PPB, spindle, and phragmoplast at different stages of the cell cycle (1, 3). We next asked whether ABS6^329−387^ associates with different MT arrays throughout the cell cycle in *Arabidopsis* root cells, taking advantage of the weak *ABS6^329−387^-GFP* OE lines in the *mRFP-TUB6* background. In interphase epidermal cells of the root elongation zone, ABS6^329−387^-GFP showed filamentous signals that merged nicely with mRFP-TUB6, consistent with our findings in hypocotyl epidermal cells, as well as cosedimentation data (Fig. 8A). In root meristematic zone, we identified cells at various mitotic stages. Overlapping ABS6^329−387^-GFP and mRFP-TUB6 signals were observed in all three types of mitotic MT arrays including PPB, spindle, and phragmoplast (Fig. 8, *B*–*D*). In addition, diffused ABS6^329−387^-GFP signals were also found in the nuclei of cells at PPB stage, indicating that it can localize to compartments other than MTs (Fig. 8B). Our data demonstrate that ABS6^329−387^-GFP is capable of labeling all types of MTs arrays *in planta*.

Discussion

In eukaryotic cells, MAPs are proteins that directly interact with MTs and modulate MT dynamics in response to internal and external signals (12). Interestingly, a growing list of land plant-specific MAPs are being identified, serving as an important adaptation to the terrestrial life after land colonization (29). We are interested in exploring the plant-specific mechanisms underlying MT dynamics and the MT basis of plant cell morphogenesis. In our previous study, we established that ABS6/AtIQD16, a member of the plant-specific IQD protein family, promotes cMT severing and ordering *via* physical and genetic interactions with the MT severing enzyme
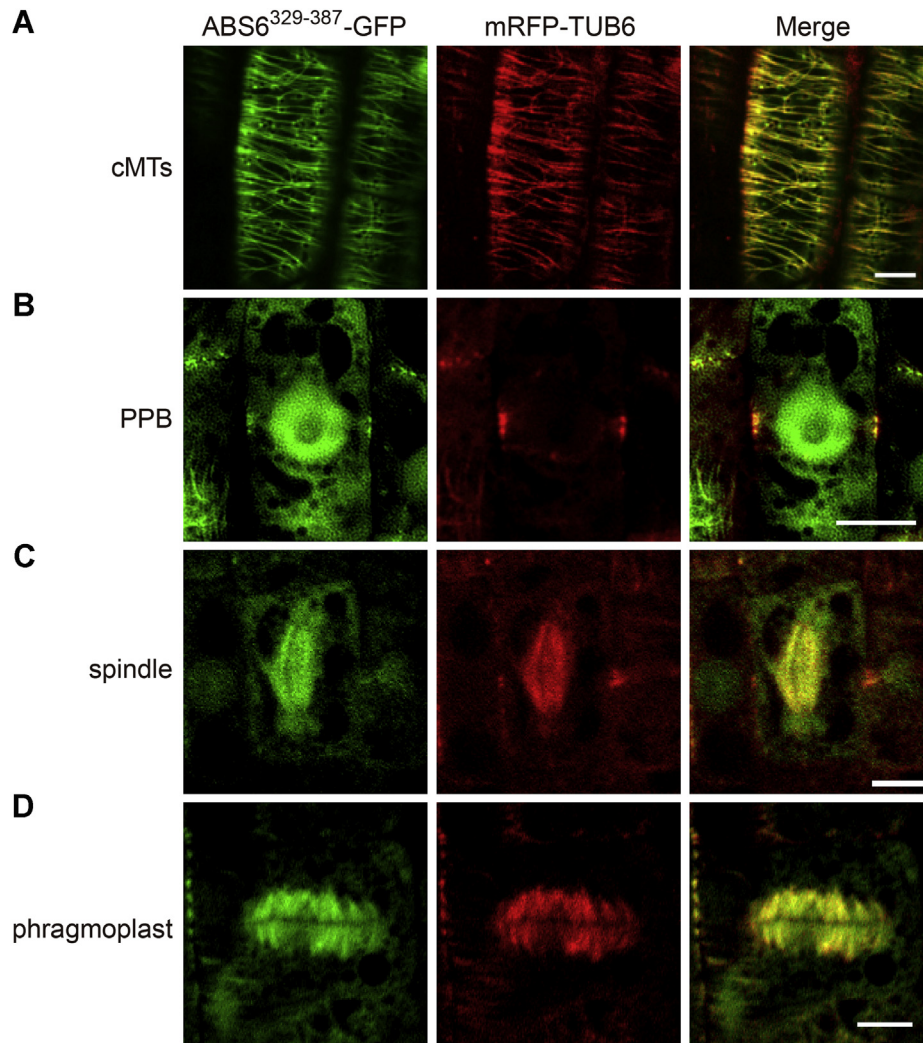
Figure 8. ABS6$^{329–387}$-GFP decorates all types of MT arrays *in planta*. *A*, cMT arrays in cells in the root elongation zone. *B–D*, PPB (*B*), spindle (*C*), and phragmoplast (*D*) MT arrays in the root meristem zone. Roots were cut from 4-day-old seedlings of weak *ABS6$^{329–387}$-GFP* OE lines in the *mRFP-TUB6* background, mounted in water, and imaged with confocal microscopy. Bars: 5 μm.

KTN1 (23). We showed that ABS6/AtIQD16 binds directly to MTs *via* its C-terminal region (23). In this study, we further pinpointed the DUF4005 domain as the MT-binding domain in ABS6 and demonstrated that when overexpressed, the DUF4005 domain is able to alter MT homeostasis and cell morphogenesis in *Arabidopsis*. *Arabidopsis* IQD family proteins were initially characterized by the presence of the IQ67 domain in their N-terminal regions (18). IQ67 domain consists of tandem repeats of IQ motifs, which presumably mediate binding to the Ca^{2+} sensor, calmodulin (CaM) (18). Indeed, calmodulin binding has been experimentally verified for several IQD proteins, including AtIQD1 and AtIQD5 (19, 22). Accumulating evidence indicates that at least a subset of IQD proteins are plant-specific MAPs and are important regulators of plant cell and organ morphogenesis (2, 19–23, 30–32). In tomato, elevated expression of *SUN/SlIQD12* as a result of a retrotransposon-mediated gene duplication underlies the elongated fruit shape (30). In rice, differential expression levels of an *IQD* gene, *GRAIN SIZE ON CHROMOSOME 5* (*GSE5*), dictated by natural variations in the promoter region of *GSE5*,

alter grain size (32). In *Arabidopsis*, increased expressions of *ABS6/AtIQD16* and *AtIQD11* lead to elongated organs, such as cotyledons and rosette leaves (23, 31). *ABS6/AtIQD16* also contributes to the robustness of apical hook formation of dark-grown seedlings in response to plant hormone ethylene (23). In addition, the loss of *AtIQD5* caused defective epidermal pavement cell morphogenesis, while AtIQD13 was shown to regulate the size and density of secondary cell wall pits (20–22). The IQD family appears to be unique to land plants, since IQD proteins have been identified in moss *Physcomitrella patens* but not in algae (33). It is interesting to note that the functions of many IQD proteins were revealed through gain-of-function and/or overexpression approaches, and more efforts need to be directed at this enigmatic protein family in land plants.

Despite the progress in understanding the molecular functions of plant IQD proteins, little is known about the interacting mechanisms between IQD proteins and MTs. The DUF4005 domain was frequently found in the C-terminal regions of plant IQD proteins. According to the Pfam database

(https://pfam.xfam.org/family/PF13178#tabview=tab0), to date, DUF4005 (Pfam ID: PF13178) has been found in 3582 protein sequences of 138 species, only one of which is from a nonplant, protist species. The vast majority of proteins containing the DUF4005 domain (3093 out of 3582) share a similar domain architecture with 1 to 3 IQ motifs in the N-terminal region and one DUF4005 domain in the C-terminal region. In the rest of DUF4005-containing proteins, DUF4005 is either stand-alone or found to be in combination with other conserved domains. Functions of these DUF4005-containing proteins are largely unknown.

Here we show that the DUF4005 domain in ABS6/AtIQD16 binds directly to MTs and tubulin *in vitro* and labels all types of plant MT arrays *in vivo* (Figs. 2 and 8). These findings indicate that the DUF4005 domain, found in the C-terminal regions of many IQD proteins, is a previously unrecognized MT-binding domain in plants. We further established that a conserved region in DUF4005, which harbors a high proportion of basic amino acid residues with a PI of 10.58, is indispensable for MT binding (Figs. 3*B* and 4, *A–C*). The C-terminal E-hook of tubulin is negatively charged and serves as an interacting platform for basic MAPs (27). Consistently, we show that DUF4005 likely binds the E-hook of tubulin through electrostatic interaction (Fig. 5). Moreover, this positively charged motif is not only conserved among IQD proteins, but also present in the C-terminal MT-binding domain of animal Kif18A homologs (Fig. 4*D*). Considering the lack of homology between ABS6 and Kif18A other than their MT-binding regions, the similarity in their MT-binding region may represent an example of convergent evolution among different types of MAPs. On the other hand, we note that the DUF4005 domain may not be the sole MT-binding domain for IQD proteins, since several MT-binding IQDs, such as AtIQD1 and AtIQD5, do not have the typical DUF4005 domain (19, 21, 22). In IQD13, three nonconsecutive regions could decorate MTs when their GFP fusions were expressed in tobacco epidermal cells (20). The third C-terminal MT-binding region in IQD13 corresponds to its DUF4005 domain (Fig. 3*A*) (20). These studies suggest diverse and complex modes of interaction between IQD proteins and MTs.

Helical growth is a rare and fascinating phenotype that has long been associated with compromised MT homeostasis in plants. Pharmacologically, low concentrations of MT destabilizer propyzamide or MT stabilizer taxol lead to left-handed spiral growth (34). Helical growth pattern is also seen in *Arabidopsis* MAP mutants. *Arabidopsis spiral1*, *2*, and *3* mutants show right-handed helical growth (34–39). SPIRAL1 (SPR1), also known as SKU6, is a plant-specific MAP belonging to a small protein family consisting of six members (SPR1 and SPIRAL1-LIKE1-5) (37, 38). The N- and C-terminal regions of SPR1/SKU6 contain two MT-binding motifs that were similar to the MT-binding motifs found in the MAP2/tau family MAPs (37, 40). SPR1/SKU6 tracks the plus-end of MTs during the growing phase and directly interacts with EB1 (38, 40, 41). SPR2, alternatively named as TORTIFOLIA1 (TOR1), defines a plant-specific MAP family with five other homologs

(35, 39). SPR2/TOR1 has one tumor overexpressed gene (TOG) domain, which is also found in MAP215 and CLASP families of MAPs (39). SPR2 is involved in regulating microtubule severing through preventing the localization of KTN1 to MT crossover sites and the protection of MT minus end (42–44). In *spr3* mutant, the causal mutation is in γ-tubulin complex protein 2 (GCP2), an essential subunit of the γ-tubulin-containing complex responsible for MT nucleation in plants (36). Temperature-sensitive conditional mutants of *MICROTUBULE ORGANIZATION 1* (*MOR1*) gene, coding for the Arabidopsis homolog of MAP215, showed left-handed twisting at restrictive temperature (45). Mutations in CSI1/POM2 also gave rise to left-handed helical growth (14). CSI1/POM2 interacts physically with both cellulose synthase and cMT, providing evidence that cMT may affect growth through its association with cellulose synthase and cell wall biogenesis (6, 14). The overexpression of *AtIQD14* can lead to left-handed helical growth (31). Interestingly, mutations of different nature in tubulin subunits can lead to both right-handed and left-handed helical growth (46–48).

Underlying the organismal helical growth are the often twisted, or oblique, arrangements of cMT arrays at the molecular level (Fig. 7*C*). Although we still do not know the molecular mechanism leading to the helical arrangement of MTs in these mutants, a helical pattern of MTs is a clear indicator of altered MT dynamics. Intriguingly, moderate overexpression of the DUF4005 domain leads to left-handed helical growth, as well as oblique arrangements of cMTs (Figs. 6 and 7). Moreover, we found that the overexpression of the DUF4005 domain causes a range of cell morphogenesis defects that correlate with the overexpression level. Taken together, the dosage-dependent effect, the small size (a peptide of only 59 amino acid residues), and the conserved nature of the DUF4005 domain of ABS6 make it a possible candidate that can be utilized to artificially perturb MT homeostasis in plants and maybe even human cells.

Experimental procedures

Plant materials and growth conditions

All *Arabidopsis* plants used are of the Columbia-0 ecotype. The MT marker line *mRFP-TUB6* has been described (24). Transgenic lines overexpressing *ABS6^{329–387}-GFP* were generated in this study. Plants were maintained at 22 °C with a continuous illumination of ~100 μmol m^{-2} s^{-1}. Plants used for protoplast preparations were maintained under 12 h/12 h day/night cycles. To analyze dark-grown seedlings, seeds were surface-sterilized, stratified in water at 4 °C in the dark for 2 days, and sown on half-strength Murashige and Skoog (MS) medium (M153, PhytoTechnology Laboratories) supplemented with 1% sucrose and 1% Bacto agar (214010, BD). Prior to the dark growth, MS plates were placed under the light for 1 h to induce germination.

DNA constructs and generation of transgenic plants

Primers used for vector construction were listed in Table S1. To express various truncated versions of ABS6 in

protoplasts, coding sequences for amino acid residues 201 to 423, 301 to 423, 329 to 387, and 387 to 423 of ABS6 were amplified and cloned into the *pTF486* vector to have GFP fused to their C-termini. The expression cassettes of GFP fusion genes in *pTF486* were under the control of the constitutive 35S promoter and the NOS terminator. To express N-terminal GST-tagged ABS6$^{329-387}$, coding sequences for amino acid residues 329 to 387 of ABS6 were amplified and cloned into *pGEX-4T-1* (27-4580-01, GE Healthcare). To generate GFP fusions of three mutated versions of ABS6$^{329-387}$, Δ(P-R), Δ(K-R), and Δ(P-S), coding sequences for the amino acid residues before and after the deleted regions were amplified and assembled with linearized *pTF486* backbone using a Gibson Assembly kit (E5510, New England BioLabs). To express N-terminal GST-tagged mutated versions of ABS6$^{329-387}$, coding sequences for Δ(P-R), Δ(K-R), and Δ(P-S) were amplified from *pTF486-Δ(P-R)*, *pTF486-Δ(K-R)*, and *pTF486-Δ(P-S)*, respectively, and cloned into *pGEX-4T-1* (27-4580-01, GE Healthcare). To overexpress ABS6$^{329-387}$-GFP in plants, the coding sequences for ABS6$^{329-387}$-GFP were amplified from the *pTF486-ABS6$^{329-387}$* vector and cloned into *pBI111L* binary vector under the control of the 35S promoter. The resulting binary vector *pBI111L-ABS6$^{329-387}$-GFP* was transformed into WT *Arabidopsis* plants *via* Agrobacterium-mediated floral dip method (49). T1 transgenic plants were screened on half-strength MS medium with 50 mg/L kanamycin.

Protoplast transient expression assay

Mesophyll protoplasts were prepared from the *mRFP-TUB6* line and transfected with indicated constructs as described (50). Protoplasts were adjusted to a concentration of 2×10^5/ml before transfection. For each transfection, 10 μg plasmid was used to transfect 100 μl protoplasts. After transfection, protoplasts were incubated for 12 h in W5 solution (2 mM MES-KOH pH5.7, 154 mM NaCl, 125 mM CaCl$_2$, and 5 mM KCl). Living protoplasts were mounted in W5 solution and directly examined with confocal microscopy after incubation.

RT-qPCR

RNAs were extracted from aerial parts of 2-week-old seedlings using the TRIzol reagent (15596026, Thermo Fisher Scientific). cDNAs were synthesized from total RNAs using the Maxima H Minus cDNA Synthesis Master Mix (M1662, Thermo Fisher Scientific). qPCRs were performed using the FastStart Essential DNA Green Master (06402712001, Roche). Expressions of *ABS6$^{329-387}$* relative to the internal control gene *ACTIN2* (*ACT2*) were calculated from three biological replicates. Primers for qPCRs were listed in Table S1.

Recombinant protein expression and purification

Expressions of GST, GST-ABS6$^{329-387}$, GST-Δ(P-R), GST-Δ(K-R), and GST-Δ(P-S) in *Escherichia coli* BL21 (DE3)

were induced with 0.1 mM IPTG at 37 °C for 4 h. After induction, GST and GST fusion proteins were purified using the Glutathione Sepharose 4B beads (17-0756-01, GE Healthcare) following the manufacture's manual. Before incubating with MTs, protein solutions were exchanged and concentrated with PEM buffer (80 mM PIPES pH 7.0, 2 mM MgCl$_2$, and 0.5 mM EGTA) using the concentrator device (88517, Pierce). Prior to MT cosedimentation assays, GST and GST fusion protein samples were subjected to 100,000g centrifugation for 15 min at 4 °C to remove aggregates with an ultracentrifuge (L-100XP, Beckman Coulter) and analyzed by SDS-PAGE followed by Coomassie Blue staining. Concentrations of GST and GST fusion proteins were determined by quantifying protein band intensities relative to the band intensities of serially diluted BSA standards loaded on the same gel.

MT cosedimentation assays

Preparation of taxol-stabilized MTs and MT cosedimentation assay were carried out using a commercial kit (BK029, Cytoskeleton, Inc). Briefly, MTs were assembled by incubating 50 μM tubulin in PEM buffer supplemented with 6% glycerol and 1 mM GTP at 35 °C for 20 min and stabilized with 20 μM taxol. In each cosedimentation assay, taxol-stabilized MTs equivalent to 2 μM tubulin were incubated with GST-tagged proteins of indicated concentrations in PEM-T buffer (80 mM PIPES pH7.0, 2 mM MgCl$_2$, 0.5 mM EGTA, and 20 μM taxol) for 20 min at room temperature. A final volume of 50 μl MT-protein mixture was loaded on top of 100 μl cushion buffer (80 mM PIPES pH7.0, 1 mM MgCl$_2$, 1 mM EGTA, 60% Glycerol, and 20 μM taxol) in a 200 μl ultracentrifuge tube and spun at 100,000g for 40 min at room temperature with an ultracentrifuge (L-100XP, Beckman Coulter). After ultracentrifugation, the top 50 μl solution in each tube was mixed with 10 μl 5× sample buffer (300 mM Tris-HCl pH6.8, 10% SDS, 50% glycerol, 0.005% bromophenol blue, and 25% v/v β-mercaptoethanol [β-ME]) and designated as the supernatant while the pellet was resuspended with 50 μl 1× sample buffer (62.5 mM Tris-HCl pH6.8, 2% SDS, 10% glycerol, 0.001% bromophenol blue, and 5% v/v β-ME). Proteins in pellets and supernatants were resolved by SDS-PAGE and stained with Coomassie Brilliant Blue.

To analyze the effect of salt on the interaction between ABS6$^{329-387}$ and MTs, cosedimentation assays were performed with taxol-stabilized MTs equivalent to 2 μM tubulin and 2 μM GST-ABS6$^{329-387}$ in PEM-T buffer supplemented with 0, 100, 250, and 500 mM NaCl. For subtilisin treatment, subtilisin (P8038, Sigma-Aldrich) from a stock (1 mg/ml in 2 mM Tris-HCl, pH8.0) was added to taxol-stabilized MTs to a final subtilisin:tubulin ratio of 1:50 (w/w). MTs were treated with subtilisin or mock-treated with equal amount of buffer for 90 min at 35 °C. Subtilisin was inactivated with 2 mM phenylmethylsulfonyl fluoride (PMSF). Cosedimentation assays were performed with subtilisin-treated or mock-treated MTs and 4 μM GST-ABS6$^{329-387}$ as described above.

Estimation of the binding affinity of ABS6$^{329-387}$ for taxol-stabilized MTs

A series of cosedimentation assays were performed with increasing concentrations of GST-ABS6$^{329-387}$ (0, 1, 2, 4, 6, 8, and 10 μM) and a fixed concentration of MTs (equivalent to 2 μM tubulin). The dissociation constant (K_d) was estimated as described (51). Briefly, after ultracentrifugation, pellets and supernatants were analyzed by SDS-PAGE. A BSA standard was also loaded onto each gel. Intensities of the GST-ABS6$^{329-387}$ bands and tubulin bands were quantified with ImageJ. Raw values of band intensities were adjusted based on sample volumes. Relative intensity of each band was normalized to the intensity of the BSA band. After subtracting the amount of GST-ABS6$^{329-387}$ present in the pellet fraction in the absence of MTs, GST-ABS6$^{329-387}$ bound to MTs (mol/mol tubulin) was calculated and plotted against the concentrations of free GST-ABS6$^{329-387}$ in the supernatant. K_d was estimated by fitting the data to the bimolecular binding equation $Y = B_{max} * X / (K_d + X)$ using nonlinear regression in GraphPad Prism 9.

GST pull-down assay

Glutathione Sepharose 4B beads (17-0756-01, GE Healthcare) were incubated with 10 μg GST or 10 μg GST-ABS6$^{329-387}$ in PEM buffer for 1 h at 4 °C. GST- or GST-ABS6$^{329-387}$-bound beads were washed with the PEM buffer for three times, incubated with 10 μg tubulin for 1 h, washed again with the PEM buffer for three times, and eluted with the elution buffer (50 mM Tris-HCl pH8.0, 10 mM reduced glutathione). All buffers used in pull-down assays were supplemented with 1 mM dithiothreitol and 1 × protease inhibitor cocktail (04693132001, Roche). Input and pull-down fractions were immunoblotted with anti-GST (ab19256, Abcam) and anti-tubulin (ab7291, Abcam) antibodies.

Microscopy

All fluorescent figures were acquired by imaging living cells. Leaf epidermal pavement cells and protoplasts were examined with a spinning disc confocal microscope (Revolution WD, Andor). Protoplasts were imaged using a 100 × oil immersion objective (HCX PL Apo 1.44 N.A., Leica). To examine pavement cell shape, cotyledons of 1-week-old seedlings were stained in 10 mg ml^{-1} propidium iodide. Abaxial side of the cotyledon was imaged using a 20 × objective (HC PL APO 0.8 N.A., Leica). MT arrays in *mRFP-TUB6* and *ABS6$^{329-387}$-GFP mRFP-TUB6* lines were examined with a laser scanning confocal microscope (Stellaris 8, Leica) using a 100 × oil immersion objective (HC PL APO CS 1.4 N.A., Leica). Plant tissues, such as cotyledons, hypocotyls of dark-grown seedlings, and roots were mounted in water for confocal imaging.

To observe the morphology of trichomes and hypocotyl epidermal cells, fifth leaves of 3-week-old light-grown plants and hypocotyls of 6-day-old etiolated seedlings were directly examined with a scanning electron microscope (FlexSEM 1000, Hitachi).

Data availability

All data presented are contained within the article.

Abbreviations—The abbreviations used are: CESA, cellulose synthase; cMT, cortical MT; DUF4005, domain of unknown function 4005; GST, glutathione S-transferase; IQD, IQ67 domain; KLCR1, kinesin light chain-related protein-1; MAP, microtubule-associated protein; MS, Murashige and Skoog; MT, microtubule; PPB, preprophase band; TRM, TON1 recruiting motif.

References

1. Elliott, A., and Shaw, S. L. (2018) Update: Plant cortical microtubule arrays. *Plant Physiol.* **176**, 94–105
2. Lazzaro, M. D., Wu, S., Snouffer, A., Wang, Y., and van der Knaap, E. (2018) Plant organ shapes are regulated by protein interactions and associations with microtubules. *Front. Plant Sci.* **9**, 1766
3. Livanos, P., and Muller, S. (2019) Division plane establishment and cytokinesis. *Annu. Rev. Plant Biol.* **70**, 239–267
4. Hamant, O., Inoue, D., Bouchez, D., Dumais, J., and Mjolsness, E. (2019) Are microtubules tension sensors? *Nat. Commun.* **10**, 2360
5. Paredez, A. R., Somerville, C. R., and Ehrhardt, D. W. (2006) Visualization of cellulose synthase demonstrates functional association with microtubules. *Science* **312**, 1491–1495
6. Gu, Y., Kaplinsky, N., Bringmann, M., Cobb, A., Carroll, A., Sampathkumar, A., Baskin, T. I., Persson, S., and Somerville, C. R. (2010) Identification of a cellulose synthase-associated protein required for cellulose biosynthesis. *Proc. Natl. Acad. Sci. U. S. A.* **107**, 12866–12871
7. Gutierrez, R., Lindeboom, J. J., Paredez, A. R., Emons, A. M., and Ehrhardt, D. W. (2009) Arabidopsis cortical microtubules position cellulose synthase delivery to the plasma membrane and interact with cellulose synthase trafficking compartments. *Nat. Cell Biol.* **11**, 797–806
8. Lindeboom, J. J., Nakamura, M., Hibbel, A., Shundyak, K., Gutierrez, R., Ketelaar, T., Emons, A. M., Mulder, B. M., Kirik, V., and Ehrhardt, D. W. (2013) A mechanism for reorientation of cortical microtubule arrays driven by microtubule severing. *Science* **342**, 1245533
9. Schaefer, E., Belcram, K., Uyttewaal, M., Duroc, Y., Goussot, M., Legland, D., Laruelle, E., de Tauzia-Moreau, M. L., Pastuglia, M., and Bouchez, D. (2017) The preprophase band of microtubules controls the robustness of division orientation in plants. *Science* **356**, 186–189
10. Ambrose, J. C., and Cyr, R. (2008) Mitotic spindle organization by the preprophase band. *Mol. Plant* **1**, 950–960

11. Smertenko, A., Assaad, F., Baluska, F., Bezanilla, M., Buschmann, H., Drakakaki, G., Hauser, M. T., Janson, M., Mineyuki, Y., Moore, I., Muller, S., Murata, T., Otegui, M. S., Panteris, E., Rasmussen, C., *et al.* (2017) Plant cytokinesis: Terminology for structures and processes. *Trends Cell Biol.* **27**, 885–894

12. Bodakuntla, S., Jijumon, A. S., Villablanca, C., Gonzalez-Billault, C., and Janke, C. (2019) Microtubule-associated proteins: Structuring the cytoskeleton. *Trends Cell Biol.* **29**, 804–819

13. Hamada, T. (2014) Microtubule organization and microtubule-associated proteins in plant cells. *Int. Rev. Cell Mol. Biol.* **312**, 1–52

14. Bringmann, M., Li, E., Sampathkumar, A., Kocabek, T., Hauser, M. T., and Persson, S. (2012) POM-POM2/cellulose synthase interacting1 is essential for the functional association of cellulose synthase and microtubules in Arabidopsis. *Plant Cell* **24**, 163–177

15. Bichet, A., Desnos, T., Turner, S., Grandjean, O., and Hofte, H. (2001) BOTERO1 is required for normal orientation of cortical microtubules and anisotropic cell expansion in Arabidopsis. *Plant J.* **25**, 137–148

16. Lin, D., Cao, L., Zhou, Z., Zhu, L., Ehrhardt, D., Yang, Z., and Fu, Y. (2013) Rho GTPase signaling activates microtubule severing to promote microtubule ordering in Arabidopsis. *Curr. Biol.* **23**, 290–297

17. Luo, D., and Oppenheimer, D. G. (1999) Genetic control of trichome branch number in Arabidopsis: The roles of the FURCA loci. *Development* **126**, 5547–5557

18. Abel, S., Savchenko, T., and Levy, M. (2005) Genome-wide comparative analysis of the IQD gene families in Arabidopsis thaliana and Oryza sativa. *BMC Evol. Biol.* **5**, 72

19. Bürstenbinder, K., Savchenko, T., Muller, J., Adamson, A. W., Stamm, G., Kwong, R., Zipp, B. J., Dinesh, D. C., and Abel, S. (2013) Arabidopsis calmodulin-binding protein IQ67-domain 1 localizes to microtubules and interacts with kinesin light chain-related protein-1. *J. Biol. Chem.* **288**, 1871–1882

20. Sugiyama, Y., Wakazaki, M., Toyooka, K., Fukuda, H., and Oda, Y. (2017) A novel plasma membrane-anchored protein regulates xylem cell-wall deposition through microtubule-dependent lateral inhibition of rho GTPase domains. *Curr. Biol.* **27**, 2522–2528.e2524

21. Liang, H., Zhang, Y., Martinez, P., Rasmussen, C. G., Xu, T., and Yang, Z. (2018) The microtubule-associated protein IQ67 DOMAIN5 modulates microtubule dynamics and pavement cell shape. *Plant Physiol.* **177**, 1555–1568

22. Mitra, D., Klemm, S., Kumari, P., Quegwer, J., Moller, B., Poeschl, Y., Pflug, P., Stamm, G., Abel, S., and Burstenbinder, K. (2019) Microtubule-associated protein IQ67 DOMAIN5 regulates morphogenesis of leaf pavement cells in Arabidopsis thaliana. *J. Exp. Bot.* **70**, 529–543

23. Li, Y., Deng, M., Liu, H., Li, Y., Chen, Y., Jia, M., Xue, H., Shao, J., Zhao, J., Qi, Y., An, L., Yu, F., and Liu, X. (2021) ABNORMAL SHOOT 6 interacts with KATANIN 1 and SHADE AVOIDANCE 4 to promote cortical microtubule severing and ordering in Arabidopsis. *J Integr. Plant Biol.* **63**, 646–661

24. Ambrose, C., Allard, J. F., Cytrynbaum, E. N., and Wasteneys, G. O. (2011) A CLASP-modulated cell edge barrier mechanism drives cell-wide cortical microtubule organization in Arabidopsis. *Nat. Commun.* **2**, 430

25. Stumpff, J., Du, Y., English, C. A., Maliga, Z., Wagenbach, M., Asbury, C. L., Wordeman, L., and Ohi, R. (2011) A tethering mechanism controls the processivity and kinetochore-microtubule plus-end enrichment of the kinesin-8 Kif18A. *Mol. Cell* **43**, 764–775

26. Weaver, L. N., Ems-McClung, S. C., Stout, J. R., LeBlanc, C., Shaw, S. L., Gardner, M. K., and Walczak, C. E. (2011) Kif18A uses a microtubule binding site in the tail for plus-end localization and spindle length regulation. *Curr. Biol.* **21**, 1500–1506

27. Lefevre, J., Chernov, K. G., Joshi, V., Delga, S., Toma, F., Pastre, D., Curmi, P. A., and Savarin, P. (2011) The C terminus of tubulin, a versatile partner for cationic molecules: Binding of tau, polyamines, and calcium. *J. Biol. Chem.* **286**, 3065–3078

28. Spittle, C., Charrasse, S., Larroque, C., and Cassimeris, L. (2000) The interaction of TOGp with microtubules and tubulin. *J. Biol. Chem.* **275**, 20748–20753

29. Nishiyama, T., Sakayama, H., de Vries, J., Buschmann, H., Saint-Marcoux, D., Ullrich, K. K., Haas, F. B., Vanderstraeten, L., Becker, D., Lang, D., Vosolsobe, S., Rombauts, S., Wilhelmsson, P. K. I., Janitza, P., Kern, R., *et al.* (2018) The chara genome: Secondary complexity and implications for plant terrestrialization. *Cell* **174**, 448–464.e424

30. Xiao, H., Jiang, N., Schaffner, E., Stockinger, E. J., and van der Knaap, E. (2008) A retrotransposon-mediated gene duplication underlies morphological variation of tomato fruit. *Science* **319**, 1527–1530

31. Bürstenbinder, K., Moller, B., Plotner, R., Stamm, G., Hause, G., Mitra, D., and Abel, S. (2017) The IQD family of calmodulin-binding proteins links calcium signaling to microtubules, membrane subdomains, and the nucleus. *Plant Physiol.* **173**, 1692–1708

32. Duan, P., Xu, J., Zeng, D., Zhang, B., Geng, M., Zhang, G., Huang, K., Huang, L., Xu, R., Ge, S., Qian, Q., and Li, Y. (2017) Natural variation in the promoter of GSE5 contributes to grain size diversity in rice. *Mol. Plant* **10**, 685–694

33. Kölling, M., Kumari, P., and Bürstenbinder, K. (2019) Calcium- and calmodulin-regulated microtubule-associated proteins as signal-integration hubs at the plasma membrane-cytoskeleton nexus. *J. Exp. Bot.* **70**, 387–396

34. Furutani, I., Watanabe, Y., Prieto, R., Masukawa, M., Suzuki, K., Naoi, K., Thitamadee, S., Shikanai, T., and Hashimoto, T. (2000) The SPIRAL genes are required for directional control of cell elongation in Aarabidopsis thaliana. *Development* **127**, 4443–4453

35. Buschmann, H., Fabri, C. O., Hauptmann, M., Hutzler, P., Laux, T., Lloyd, C. W., and Schaffner, A. R. (2004) Helical growth of the Arabidopsis mutant tortifolia1 reveals a plant-specific microtubule-associated protein. *Curr. Biol.* **14**, 1515–1521

36. Nakamura, M., and Hashimoto, T. (2009) A mutation in the Arabidopsis gamma-tubulin-containing complex causes helical growth and abnormal microtubule branching. *J. Cell Sci.* **122**, 2208–2217

37. Nakajima, K., Furutani, I., Tachimoto, H., Matsubara, H., and Hashimoto, T. (2004) SPIRAL1 encodes a plant-specific microtubule-localized protein required for directional control of rapidly expanding Arabidopsis cells. *Plant Cell* **16**, 1178–1190

38. Sedbrook, J. C., Ehrhardt, D. W., Fisher, S. E., Scheible, W. R., and Somerville, C. R. (2004) The Arabidopsis sku6/spiral1 gene encodes a plus end-localized microtubule-interacting protein involved in directional cell expansion. *Plant Cell* **16**, 1506–1520

39. Shoji, T., Narita, N. N., Hayashi, K., Asada, J., Hamada, T., Sonobe, S., Nakajima, K., and Hashimoto, T. (2004) Plant-specific microtubule-associated protein SPIRAL2 is required for anisotropic growth in Arabidopsis. *Plant Physiol.* **136**, 3933–3944

40. Galva, C., Kirik, V., Lindeboom, J. J., Kaloriti, D., Rancour, D. M., Hussey, P. J., Bednarek, S. Y., Ehrhardt, D. W., and Sedbrook, J. C. (2014) The microtubule plus-end tracking proteins SPR1 and EB1b interact to maintain polar cell elongation and directional organ growth in Arabidopsis. *Plant Cell* **26**, 4409–4425

41. Balkunde, R., Foroughi, L., Ewan, E., Emenecker, R., Cavalli, V., and Dixit, R. (2019) Mechanism of microtubule plus-end tracking by the plant-specific SPR1 protein and its development as a versatile plus-end marker. *J. Biol. Chem.* **294**, 16374–16384

42. Wightman, R., Chomicki, G., Kumar, M., Carr, P., and Turner, S. R. (2013) SPIRAL2 determines plant microtubule organization by modulating microtubule severing. *Curr. Biol.* **23**, 1902–1907

43. Fan, Y., Burkart, G. M., and Dixit, R. (2018) The Arabidopsis SPIRAL2 protein targets and stabilizes microtubule minus ends. *Curr. Biol.* **28**, 987–994.e983

44. Nakamura, M., Lindeboom, J. J., Saltini, M., Mulder, B. M., and Ehrhardt, D. W. (2018) SPR2 protects minus ends to promote severing and reorientation of plant cortical microtubule arrays. *J. Cell Biol.* **217**, 915–927

45. Whittington, A. T., Vugrek, O., Wei, K. J., Hasenbein, N. G., Sugimoto, K., Rashbrooke, M. C., and Wasteneys, G. O. (2001) MOR1 is essential for organizing cortical microtubules in plants. *Nature* **411**, 610–613

46. Buschmann, H., Hauptmann, M., Niessing, D., Lloyd, C. W., and Schaffner, A. R. (2009) Helical growth of the Arabidopsis mutant tortifolia2 does not depend on cell division patterns but involves handed twisting of isolated cells. *Plant Cell* **21**, 2090–2106

47. Thitamadee, S., Tuchihara, K., and Hashimoto, T. (2002) Microtubule basis for left-handed helical growth in Arabidopsis. *Nature* **417**, 193–196

48. Ishida, T., Kaneko, Y., Iwano, M., and Hashimoto, T. (2007) Helical microtubule arrays in a collection of twisting tubulin mutants of Arabidopsis thaliana. *Proc. Natl. Acad. Sci. U. S. A.* **104**, 8544–8549

49. Clough, S. J., and Bent, A. F. (1998) Floral dip: A simplified method for agrobacterium-mediated transformation of Arabidopsis thaliana. *Plant J.* **16**, 735–743

50. Yoo, S. D., Cho, Y. H., and Sheen, J. (2007) Arabidopsis mesophyll protoplasts: A versatile cell system for transient gene expression analysis. *Nat. Protoc.* **2**, 1565–1572

51. Alberico, E. O., Duan, A. R., and Goodson, H. V. (2017) Measuring tau-microtubule affinity through cosedimentation assays. *Methods Cell Biol.* **141**, 115–134